Chiral Chemistry
https://doi.org/10.70401/cc.2026.0021

Supplementary information

Pyrite interference in prebiotic chiral selection of amino acids

Ruiqi Li, Quanzheng Deng, Lu Han, Yingying Duan, Tianwei Ouyang, Mengyi Wei, Yuxi Fang

Materials

Natural pyrite (NP) was purchased from Alfa Aesar Shanghai. Synthesized pyrite (SP) (99%) was purchased from Shanghai Aladdin Biochemical Technology Co., Ltd.

$FeCl_2 \cdot 4H_2O$ (99%), pyruvic acid (99%), N^{α}-(5-Fluoro-2,4-dinitrophenyl)-L-leucinamide (98 %), L-Phe (99%) and D-Phe (98%) were purchased from TCI Shanghai. D-Pen (99 %), L-Ser (99%), D-Ser (99%), L-Val (99%) and D-Val (98%) were purchased from Shanghai Aladdin Biochemical Technology Co., Ltd. L-Pen (98%) was purchased from J&K Scientific Co., Ltd. Ammonium hydroxide solution (25~28% aqueous solution), ammonium bicarbonate (99 %), $KMnO_4$ (99%), *n*-butanol (99%) and acetone (99.5 %) were purchased from Sinopharm Chemical Reagent Co., Ltd. The deionized (DI) water (resistivity ~18.2 MΩ cm) was obtained from a Milli-Q synthesis system. All chemicals were directly used without further purification.

The permanent magnets with central magnetic field strengths of 0.5 T and 1.0 T were designed and assembled by Lane Chuangzhi Strong Magnetic Manufacturing (Shenzhen) Co., Ltd. The permanent magnet with a central magnetic field strength of 1.5 T was purchased from JASCO Corporation.

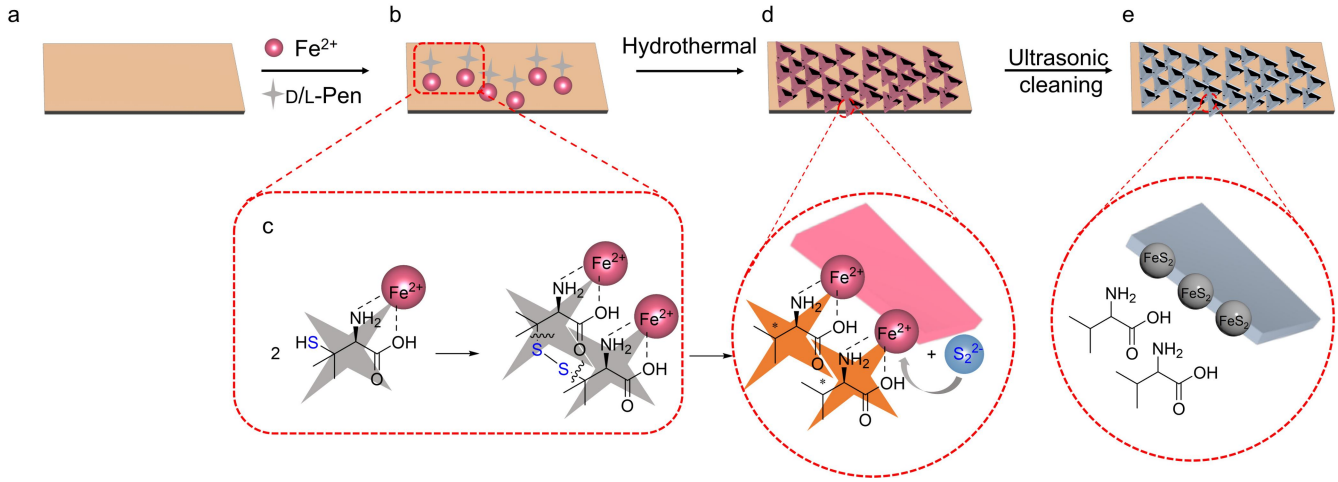

Figure S1. Schematic illustration for the synthesis of CMP. a, Activated FTO substrate. **b,** Formation of Fe-Pen complexes in a mixture solution of $FeCl_2 \cdot 4H_2O$ and D/L-Pen. **c,** The possible mechanism of S_2^{2-} generation from the Fe-Pen complex in a hydrothermal environment. **d,** Growth of CMP on FTO substrate during a hydrothermal process under 180 °C. e, The residue of organics was removed by washing to obtain pure CMP.

D/L-Pen was selected as both the symmetry-breaking agent and the sulfur source. At room temperature, Pen coordinates with Fe^{2+} ions in the solution to form Fe^{2+}-Pen complex (Figure S1b). During the hydrothermal reaction, as the temperature increases, Pen undergoes dimerization to form $(Fe^{2+}\text{-Pen})_2$. At higher temperatures, $(Fe^{2+}\text{-Pen})_2$ begins to decompose, releasing S_2^{2-}. The asymmetric arrangement of Fe-NH_2 and Fe-COOH bonds around the chiral carbon center regulates the oriented, misaligned growth of nanocrystals, ultimately leading to the formation of chiral nanosheets. Simultaneously, S_2^{2-} reacts with Fe^{2+} to produce FeS_2 (Figure S1d). The Val formed from the decomposition of Pen in the mother liquor underwent a racemization reaction, resulting in the formation of Rac-Val (*vide post*). Pure CMP was obtained after three cycles of ultrasonic cleaning with deionized water and anhydrous ethanol, respectively (Figure S1e).

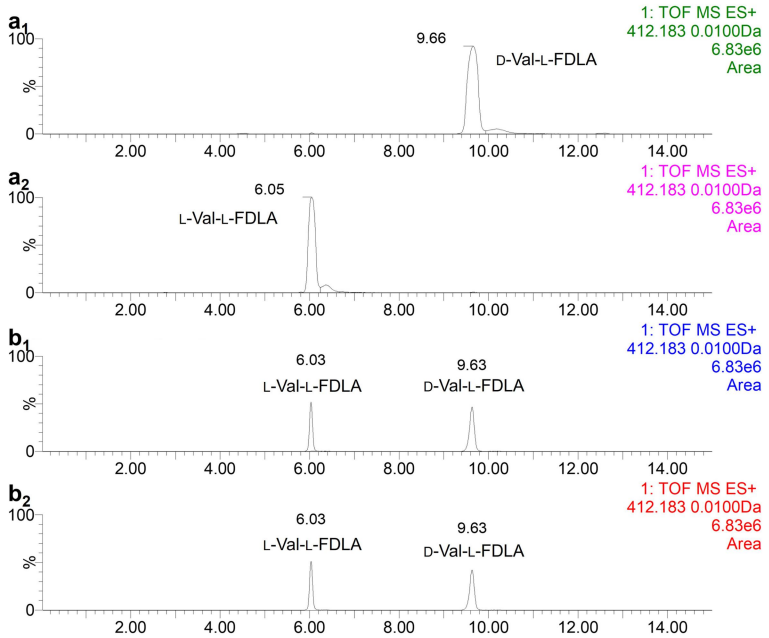

Figure S2. a$_{1\text{-}2}$, HPLC-MS of standard D- (a_1) and L-Val (a_2) derivatized by L-FDLA. **b$_{1\text{-}2}$,** HPLC-MS of the residual organics in the supernatant derivatized by L-FDLA after synthesis of D- (b_1) and L-CMP (b_2).

To investigate the transformation of Pen during CMP formation, we analyzed the residual organics in the supernatant after hydrothermal synthesis of CMP. The supernatant was derivatized with L-FDLA and analyzed by HPLC-MS (Figure S2b$_{1\text{-}2}$). The HPLC-MS results, which showed the same peak position as the standard Val (Figure S2a$_{1\text{-}2}$), revealed a significant amount of Val in the reaction solution. These results indicate that Pen induce the chiral structure of pyrite while sulfide the Fe^{2+} to form pyrite.

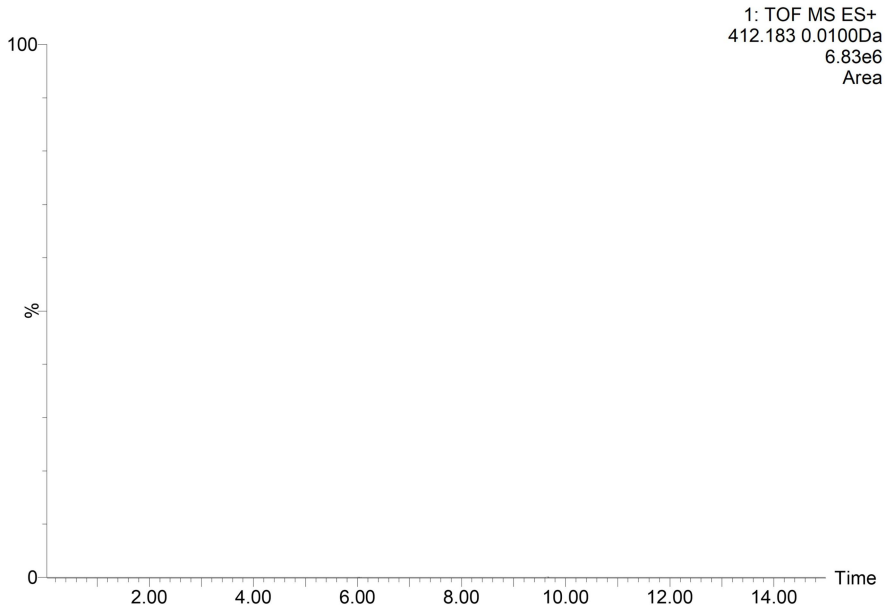

Figure S3. The HPLC-MS of D-CMP dissolved in the nitric acid solution.

To confirm the absence of residual chiral molecules in the washed CMP, CMP was dissolved in a 1 M nitric acid solution, derivatized with L-FDLA, and analyzed by HPLC-MS. The HPLC-MS results showed no amino acid peak in the D-CMP solvent, indicating that the amino acids in CMP were completely removed during washing.

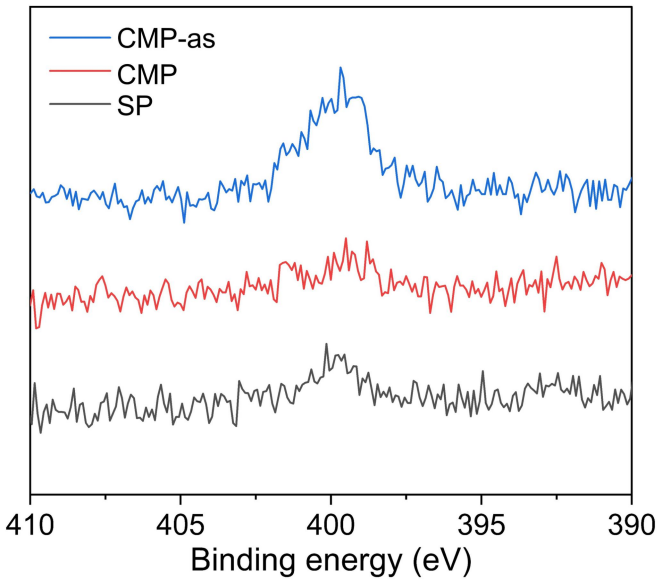

Figure S4. N 1s high-resolution XPS of D-CMP-as (before washing), D-CMP (after washing) and SP.

To further confirm the absence of residual chiral molecules in the washed CMP, XPS analysis was conducted on the surfaces of D-CMP-as (before washing), D-CMP (after washing), and on the SP. As shown in Figure S4, a significant N 1s peak at *ca.* 399.4 eV was observed in D-CMP-as. The weak peaks in same position observed in SP probably attributed to the N_2 in air. XPS spectra of D-CMP after washing show that the intensity of N 1s peak located at 399.4 eV corresponding to the N element of amino acids is almost the same as that of SP synthesized without amino acids. This result also revealed that amino acids was completely removed by washing.

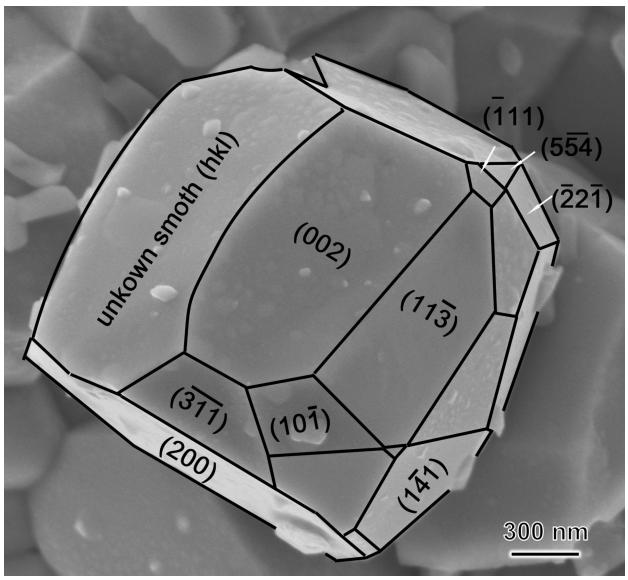

Figure S5. Analysis of the exposed crystal planes of SP nanoparticles.

Pyrite belongs to the m3 point group. SEM image analysis shows that the dominant exposed crystal planes of SP are low-index facets such as {200}, {111}, {311}, and {221} (Figure S5), indicating that these surfaces likely serve as the primary active sites in the catalytic reactions.

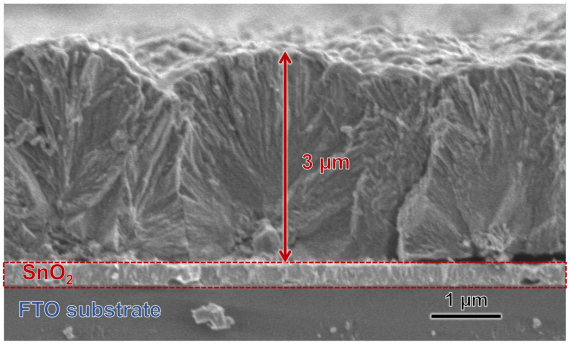

Figure S6. SEM images of D-CMP from side views. The height of D-CMP grown on FTO was measured to be *ca.* 3 μm.

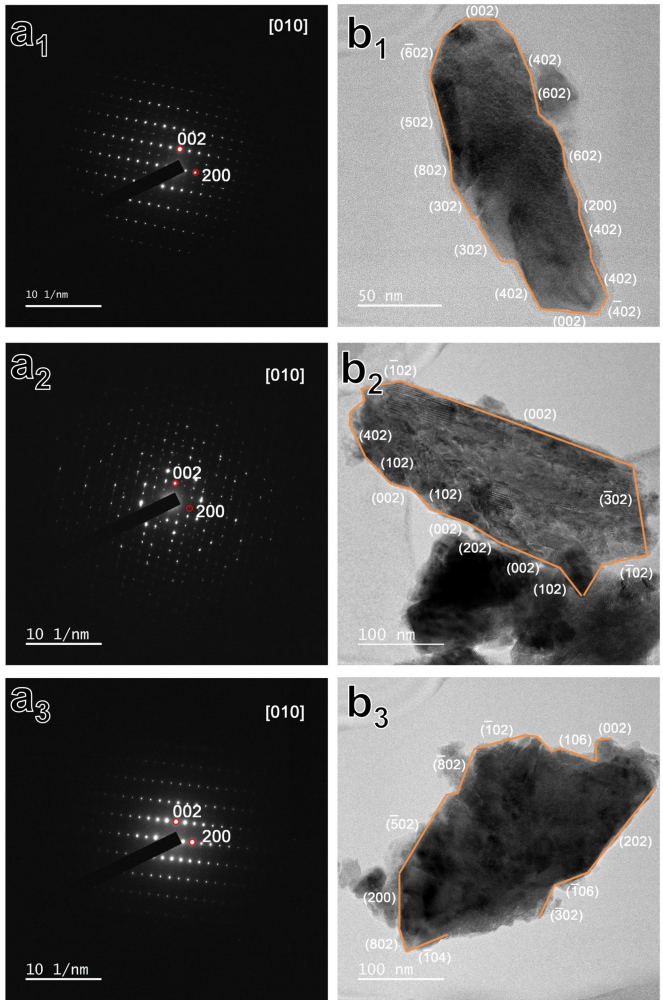

Figure S7. Structure of D-CMP. **a**$_{1\text{-}3}$, The selected area electron diffraction (SAED) images of D-CMP. **b**$_{1\text{-}3}$, TEM images of D-CMP.

TEM and SAED images of multiple D-CMP particles prove that crystal surfaces such as {200}, {102}, {302} and {402} are exposed, which would most likely act as adsorption and catalytic sites in most natural pyrite particles.

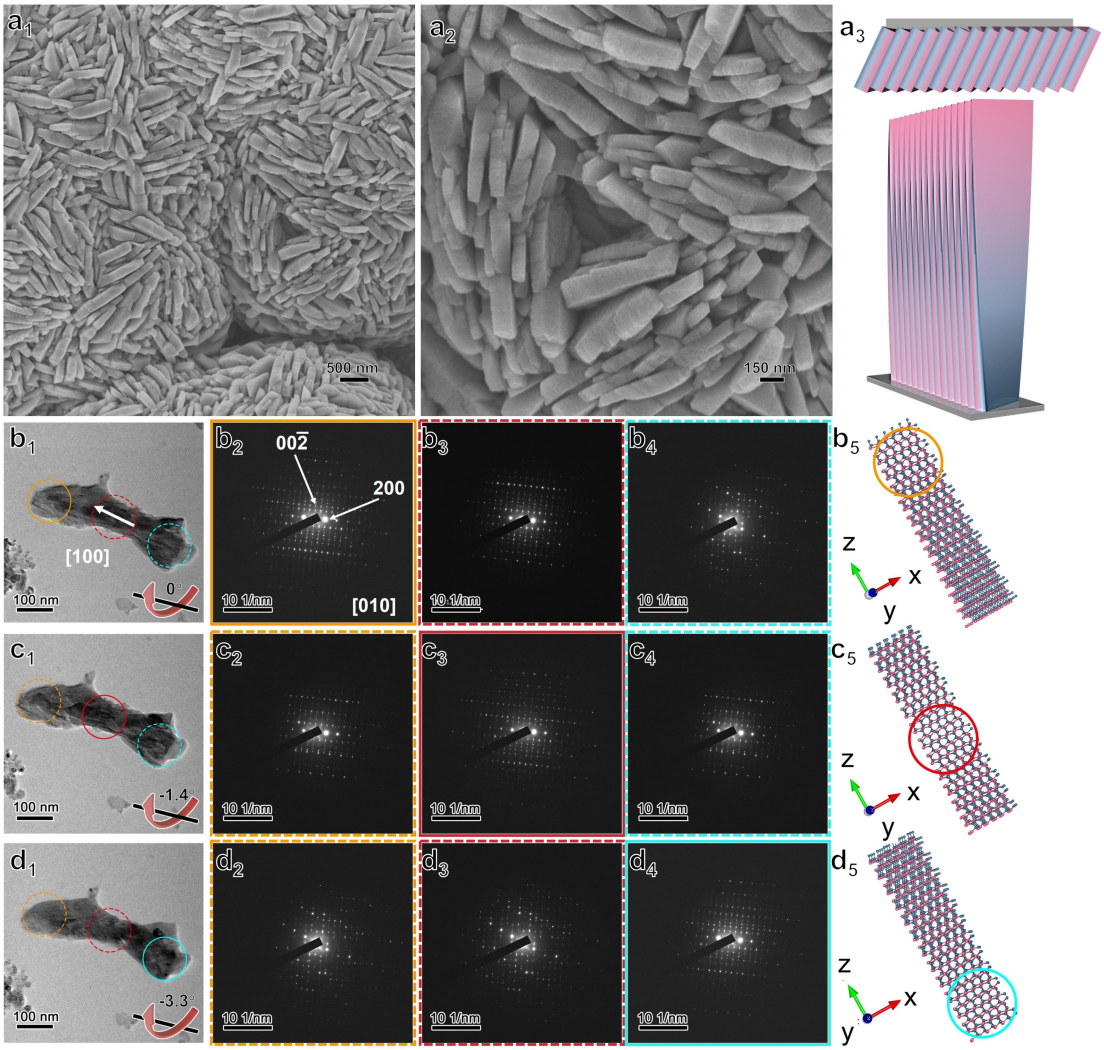

Figure S8. SEM images (**a**$_{1\text{-}2}$), TEM images(**b**$_1$-**d**$_1$), corresponding SAED patterns and schematic crystal structure models L-CMP with left-handed form. The [100] axis in the nanoflakes (b-d) can only be aligned to the incident electron beam in the top region (orange circle); by tilting the nanoflakes along the [100] axis by -1.4° and -3.3°, the middle region (red circle) and bottom region (cyan circle) can be well aligned, respectively. The synthetic molar composition was 1.5 L-Pen: 0.5 $FeCl_2$•H_2O: 2222 H_2O.

The D-CMP and L-CMP and exhibit similar morphology, with densely assembled nanoflakes showing a uniform structure. In D- and L-CMP, nanoflakes with a thickness of approximately 100 nm and lengths of 500-700 nm are clearly observed to be arranged in a rotating pattern, indicating the presence of a helical distortion structure (Figure S8a).

The TEM images and the corresponding selected area electron diffraction (SAED) patterns of L-CMP in Figure S8b-d reveal the crystal orientation with continuous tilting. When the incident electron beam was aligned to the [100] axis for the top area (indicated by the orange circle) of the nanoflake, the zone axis was deflected in the middle (indicated by the red circle) and bottom (indicated by the cyan circle) regions. By tilting the sample along the [100] direction at -1.4° and -3.3°, the SAED patterns of the middle and bottom sections, respectively, were in good alignment, illustrating that the crystal structure of the L-CMP nanoflakes was twisted along the [100] direction in the right-handed form.

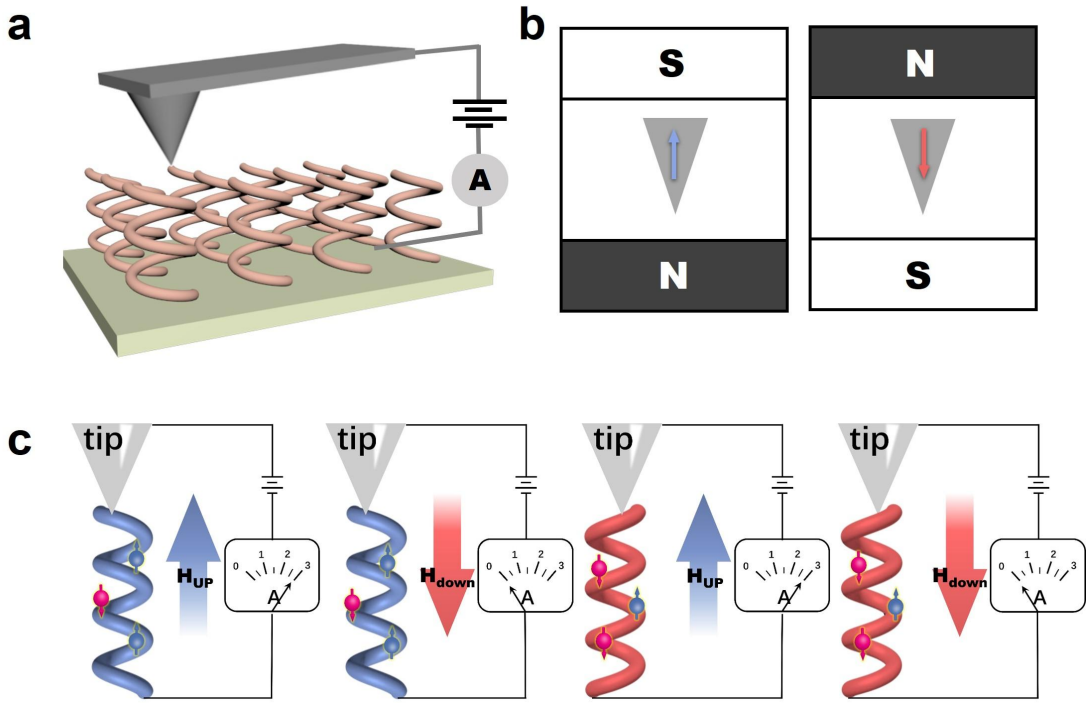

Figure S9. Schematic representation for magnetic conducting atomic force microscopy (mc-AFM) measurements. **a,** The experimental setup involved using a magnetic Pt-coated Cr tip (Multi75E-G, Budget Sensors) with nominal spring constant 3 N/m was used to acquire I-V curves. **b,** The tips are pre-magnetized using a 1.6 T permanent magnet. When the tip pointed to the north pole of the magnet, it is magnetized in the UP direction. Conversely, when the tip pointed to the south pole of the magnet, it is magnetized in the DOWN direction. **c,** Schematic illustration of the parallel configuration with a high tunneling current and antiparallel configuration with a low tunneling current between the tip and film. The electron was depicted as a sphere, with the arrow indicating its spin.

When a bias potential is applied, the transfer of electrons from the substrate to the tip can generate an electric current. The current-voltage (I-V) curves, depending on the direction of tip magnetization (UP or DOWN relative to substrate), can reflect the spin polarity of the tunneling carriers.

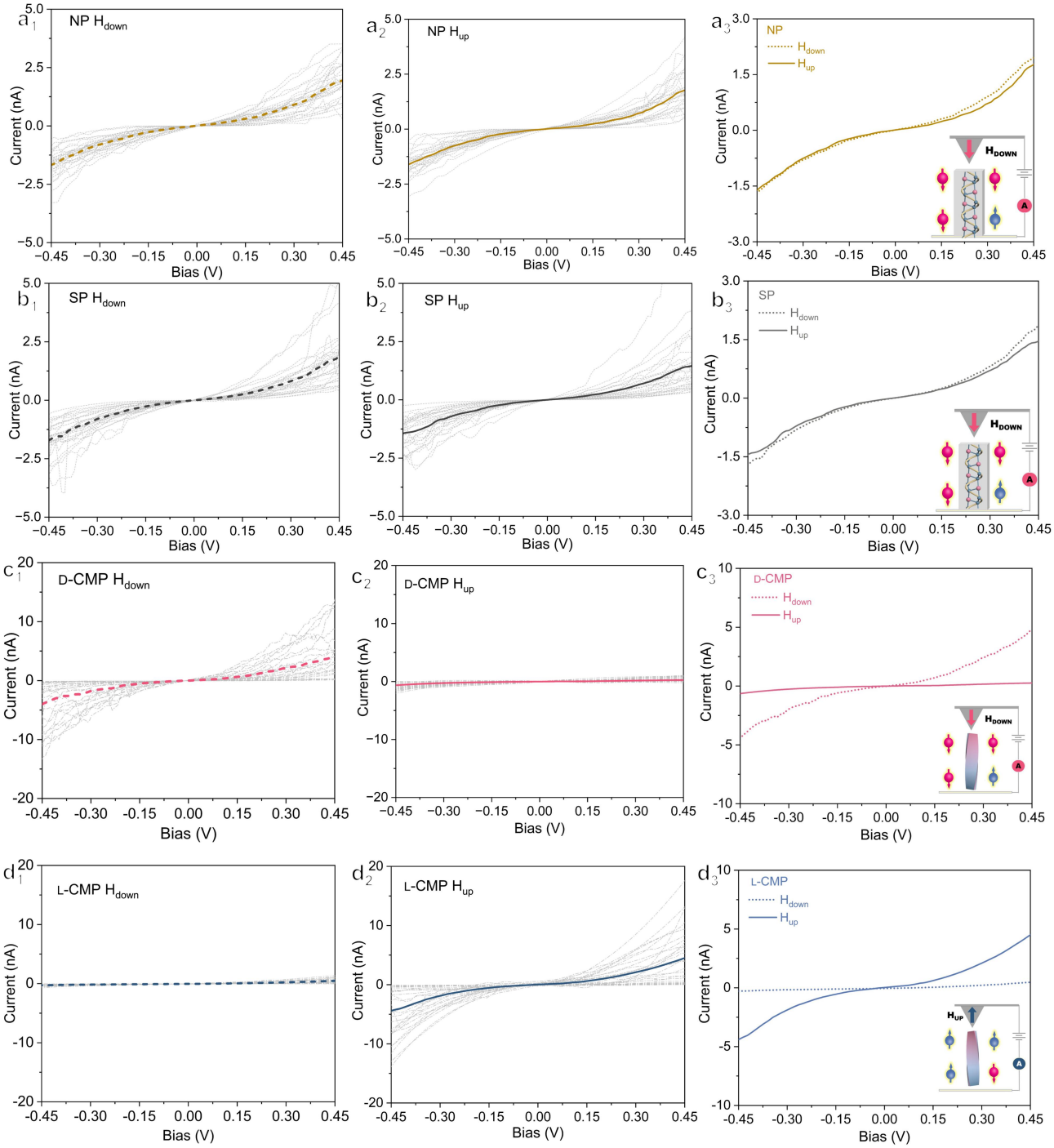

Figure S10. I-V curves obtained from NP, SP and D-/L-CMP using mc-AFM.

Around 25 I-V curves of NP, SP and D-/L-CMP were recorded and averaged with the tips magnetized in the DOWN and UP directions (Figure S10). Each I-V curve was obtained at different points on the sample. The slight dependence of the current on the orientation of magnetization at the tip of the mc-AFM for NP and SP confirms their spin polarization, with spin DOWN in both NP and SP. The opposite dependence of the current on the orientation of magnetization at the tip of the mc-AFM for the antipodal CMP confirms the opposite spin polarization, spin DOWN and UP in D- and L-CMP, respectively.

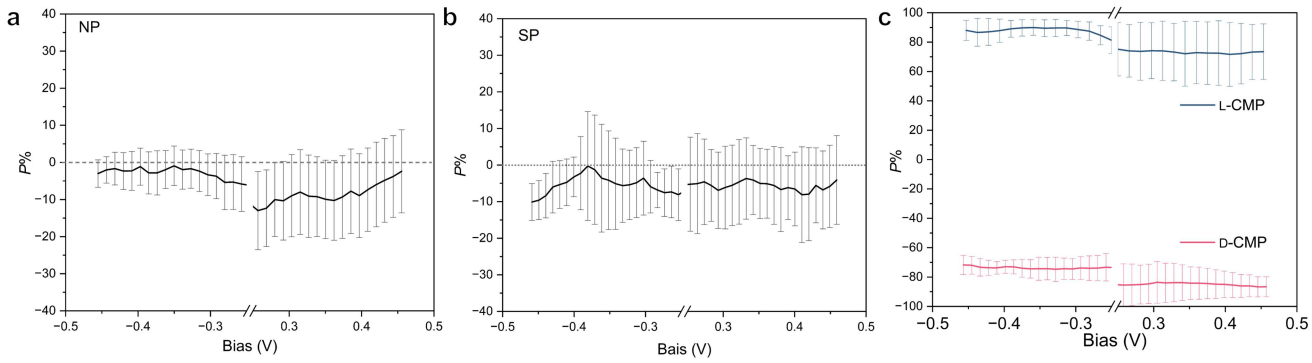

Figure S11. Spin polarization versus bias voltage curves of NP (**a**), SP (**b**) and antipodal CMP (**c**). As both the I_{UP} and I_{DOWN} were almost zero in the bias voltage of -0.25~0.25 V, the spin polarization was not inaccurate. The curves in this range were substituted with the symbol //.

The degree of spin polarization P is the physical quantity evaluating spin polarization:

$$P = (I_{UP} - I_{DOWN})/(I_{UP} + I_{DOWN}) \times 100\%$$

Where I_{UP} and I_{DOWN} represent the currents measured at the tip magnetized in the UP and DOWN direction, respectively. The spin polarization degrees of NP and SP were consistently negative, ranging from -1.33% to -12.95% for NP and -0.25% to -10.09% for SP, with average values of approximately -5.62% and -5.55%, respectively. In contrast, the spin polarization degrees of D- and L-CMP were more pronounced, ranging from -87.55% to -65.42% for D-CMP and from 71.52% to 90.04% for L-CMP, with average values of -78.9% and +79.9%, respectively.

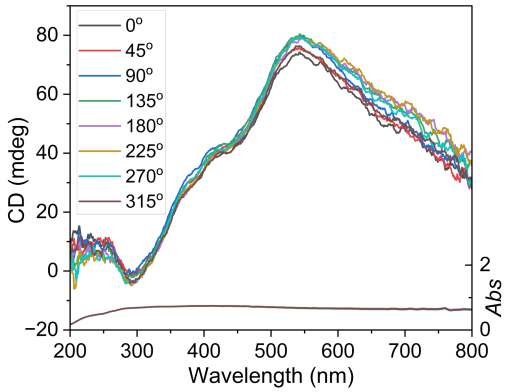

Figure S12. DRCD and DRUV−vis spectra of the D-CMP measured at different angles by rotating the sample with the direction of incident light as the axis.

The coincident CD spectra at different angles demonstrate that the artifact attributed to LD is negligible.

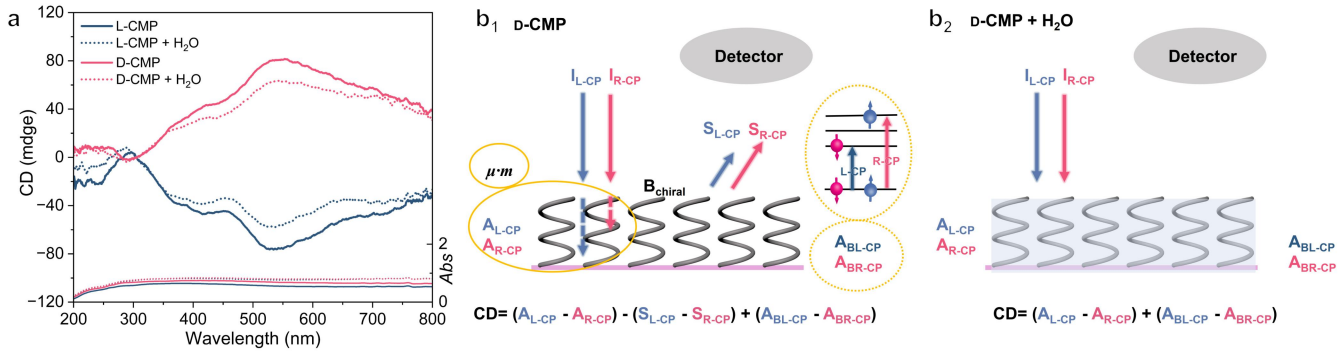

Figure S13. DRCD and DRUV-Vis spectra of antipodal CMPs without and with infiltration of water (**a**) and schematic diagram of the circular polarization selectivity of D-CMP (**b**$_1$) and D-CMP with infiltration of water (**b**$_2$). $A_{L\text{-}CP}$ and $A_{R\text{-}CP}$ represent the absorption of L- and R-CPL by D-CMP, respectively, with intensities indicated by dashed lines. $A_{BL\text{-}CP}$ and $A_{BR\text{-}CP}$ denote the absorption of L- and R-CPL resulting from energy splitting induced by $\mathbf{B}_{chiral}$, illustrated as energy level diagrams. $S_{L\text{-}CP}$ and $S_{R\text{-}CP}$ represent the scattering of L- and R-CPL by D-CMP, respectively, with intensities indicated by solid lines.

As shown in Figure S13, the CD spectra of antipodal CMPs saturated with air and water both exhibit mirror-imaged CD lines, but with different intensities, indicating the opposite chiral structures in antipodal CMPs and resulting in absorption-based OA (AOA), scattering-based OA (SOA). AOA is composed of Natural CD (NCD) and $\mathbf{B}_{chiral}$ induced CD.

As shown in Figure S13b$_1$, the DRCD signals of CMP were confirmed as the superposition of three circular dichroic sources:

(i) NCD signals ($\boldsymbol{\mu}\bullet\boldsymbol{m}$) arise from charge net redistribution due to electron transition from VB to CB. In classical AOA model, the electric and magnetic fields of CPL drive electric charges along a helical structure in two ways: directly *via* the electric field and indirectly *via* current induced by the time-varying magnetic field. These effects are in phase for one CPL handedness and out of phase for the other, resulting in different current magnitudes and thus differential electron transition absorption-based CD. The CD power dissipation is given by: $CD = \frac{\sigma a L r \omega E_0^2}{2c} cos\theta sin\theta$, where σ is the electrical conductivity of the helical wire, a is the cross-sectional area of this wire, L is the total helix path length corresponding to the height of helix, ω and E_0 are the temporal frequency and wave amplitude of incident CPL, θ is the pitch angle. CD is maximized at $\theta = 45°$, and vanishes when the helix is a straight rod ($\theta = 0$) or a flat circle ($\theta = \pm\pi/2$). The CD signal is positive for right-handed helices and negative for left-handed ones[1,2].

(ii) CD signals can be generated from spin polarization induced by $\mathbf{B}_{chiral}$ due to the movement of electrons in a helical potential. As a result of spin orbit coupling ($\boldsymbol{\mu}_s\bullet\ \mathbf{B}_{chiral}$), one spins were stabilized while the other destabilized. In D-CMP with DOWN spins stabilized, L-CPL were predominantly absorbed, resulting in positive CD signal, and *vice versa* in L-CMP.

(iii) Scattering-based CD signals arise from the circular Bragg resonance. The circular Bragg resonance occurs on structurally chiral materials, which can be engineered for any wavelengths. These materials tend to reflect

the CP photons of one handedness and transmit the other when the helical pitch of the structures is of the same order as the wavelength of the incident electromagnetic wave according to the relation:

$$m\lambda = Pn_{average}\, sin\, \alpha$$

where λ is the wavelength, P is the pitch length, $n_{average}$ is the effective average refractive index of the medium and environments, and α (alpha) is the angle between the incident light and the surface of the chiral film. The SOA signal of chiral films could be decreased by saturation with some isotropic molecules (such as water). This effect may be attributed to approximate refractive matching between the isotropic molecules and the film resulting in a reversible disappearance of the optical chiral interface and a decrease in SOA. According to CD spectra of antipodal CMPs saturated with air and water, it can be deduced that D-CMP with right-handed structures and dominantly reflected R-CPL, resulting in positive CD signal in DRCD measurements, and *vice versa* in L-CMP.

Briefly, AOA signals including NCD and CD induced by $\mathbf{B}_{chiral}$ in CMPs show significant overlapping, leading to challenge for discussing orientation of chiral structures in CMPs. Based on the SOA, the right-handed chiral structures in D-CMP and left-handed structures in L-CMP can be confirmed, which is consistent with TEM observation.

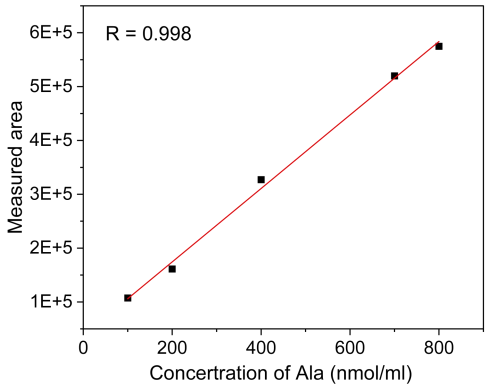

Figure S14. Calibration curves for the quantification of Ala by HPLC-MS analysis using L-FDLA derivatization were constructed. The standard curve was prepared by using a series of concentrations of Ala derivatized with L-FDLA aqueous solution.

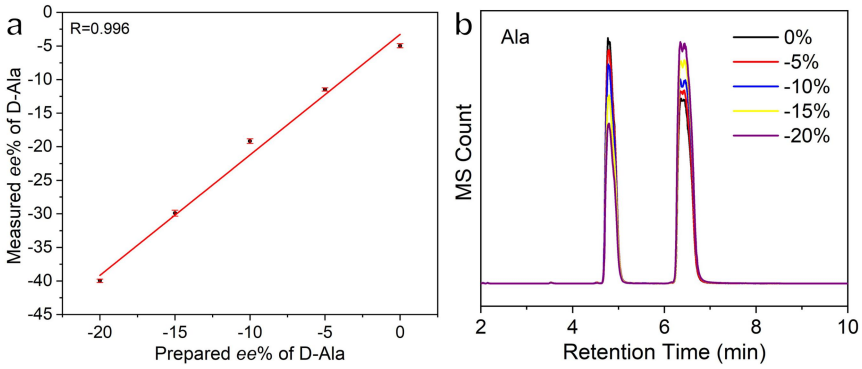

Figure S15. Calibration curves of HPLC-MS analysis for Ala by L-FDLA derivatization. a, Standard curve constructed by using a series of *ee* value of Ala aqueous solutions. All experiments were independently conducted three times, and the mean value was taken as the final result. **b**, HPLC-MS of Ala with series of *ee* values. Error bars correspond to the standard deviations calculated by performing three independent measurements.

The standard curves were prepared as follows: Ala is configured as a standard solution of a series of *ee* values at a concentration of 7 μmol/ml，50 μl of an aqueous solution was mixed with 20 μl of 200 mM sodium bicarbonate and 20 μl of 1 % L-FDLA in acetone. The mixture was incubated at 37 °C for 30 min. After returning to room temperature, 200 μl of methanol was added to the sample, and the impurity was centrifuged (12000 rpm, 10 min). The derivatized solution was analyzed by HPLC-MS and a standard curve was constructed by linear fit based on standard *ee* values and measurements. All experiments were independently conducted three times, and the mean value was taken as the final result.

The yields of Ala were corrected using the corresponding standard curve (Figure S14). To eliminate the chiral bias of the L-FDLA derivatization method for amino acid enantiomers, *ee* values were corrected using the corresponding standard curve (Figure S15).

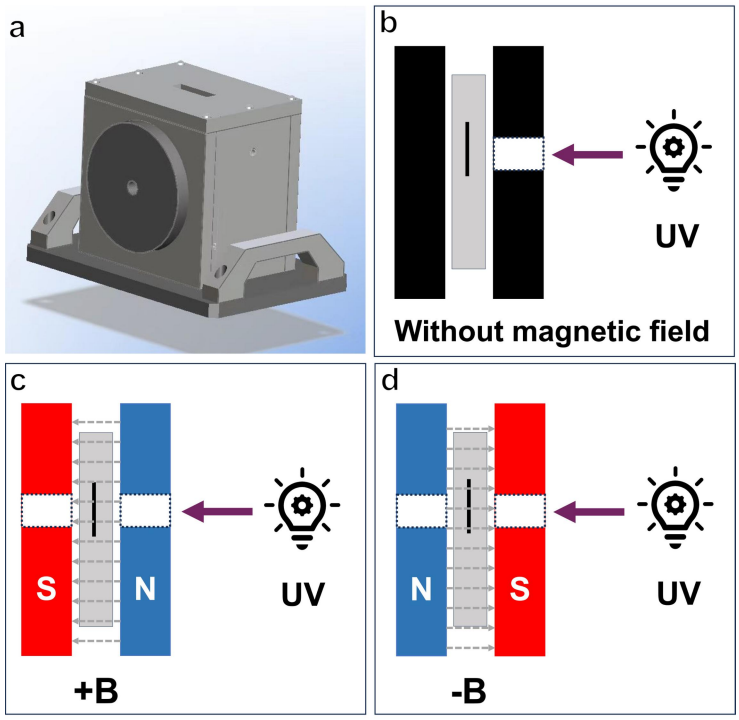

Figure S16. a, The permanent magnet model used in the photocatalytic experiments. **b,** Schematic diagram of the photocatalytic reaction setup without an external magnetic field, where a baffle with the same aperture as the permanent magnet is placed between the reaction vessel and the UV lamp to ensure uniform light exposure in the reaction system. **c, d,** Schematic diagrams of the photocatalytic reaction setup with an external magnetic field, where the magnetic field is aligned either parallel (**c**) or antiparallel (**d**) to the light direction, labeled as **+B** or **-B**, respectively.

As shown in Figure S16a, an external magnetic field was applied to the photocatalytic reaction system using a permanent magnet. The permanent magnet device consists of two strong magnets, each with a 1 cm diameter light aperture, with a 10 mm gap between the magnets. The three magnets used in this study generate central magnetic fields of 0.5 T, 1.0 T, and 1.5 T. The photocatalytic reaction was conducted in a quartz cuvette with a 5 mm light path, with the catalyst fixed in place to ensure it was irradiated by the UV lamp through the light aperture when positioned within the magnetic field. The polarity of the external magnetic field can be easily reversed by changing the orientation of the permanent magnets (Figure S16c,d). During the reaction, the

reaction vessel was manually shaken for 10 seconds every 15 minutes to facilitate the reaction. For comparison, the photocatalytic reaction without an external magnetic field was performed in a similar manner (Figure S16b), with light exposure controlled using a baffle with the same aperture and the same manual shaking procedure.

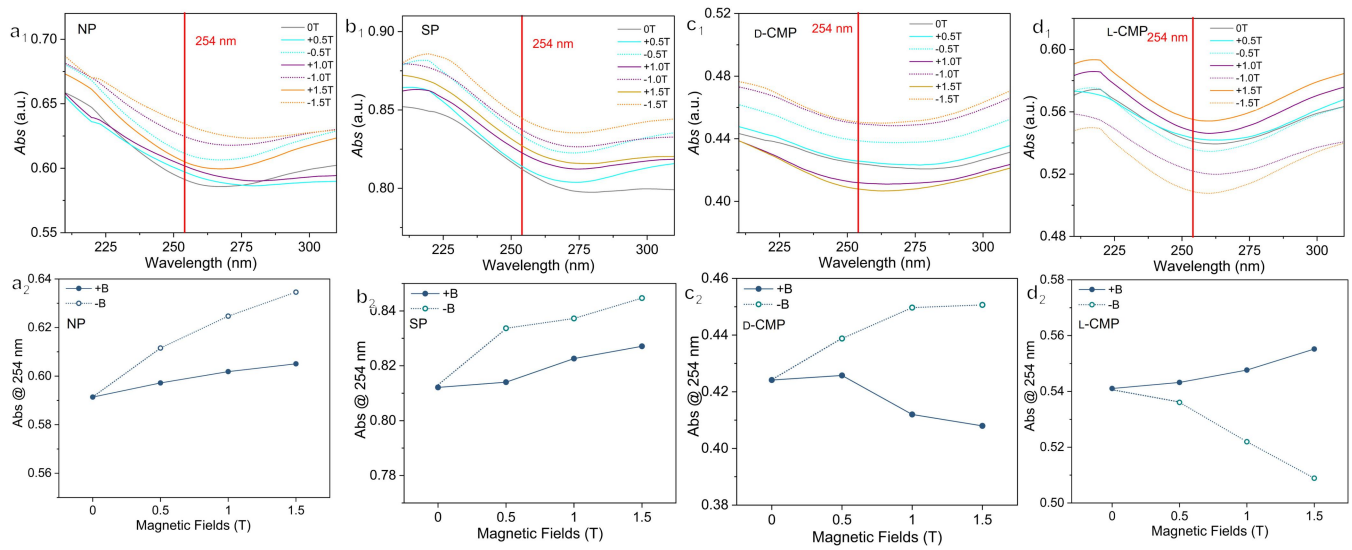

Figure S17. a_1-d_1, UV-vis absorption spectra of NP (a_1), SP (b_1), D- and L-CMP (c1 and d1) at 25 °C applied with different external magnetic fields. a_2-d_2, The Absorbance (Abs) of NP (a_2), SP (b_2), D- and L-CMP (c_2 and d_2) at 254 nm under different external magnetic fields.

Adsorption spectra analysis was conducted on optically transparent thin films formed by evenly dispersing NP, SP and CMP on quartz plates. Figure S17 displays the absorption spectra of NP, SP, D- and L-CMP under different magnetic field strengths. The absorption curve at 0 T is shown as a gray solid line, while the absorption curves under +**B** and -**B** are represented by colored solid and dashed lines, respectively.

As shown in Figure S17 a_2-d_2, the Abs at 254 nm for both NP and SP increase under +**B**, while it increases significantly under -**B**. For D-CMP, the Abs at 254 nm significantly decreases under +**B** and increases under -**B**, and *vice versa* for L-CMP.

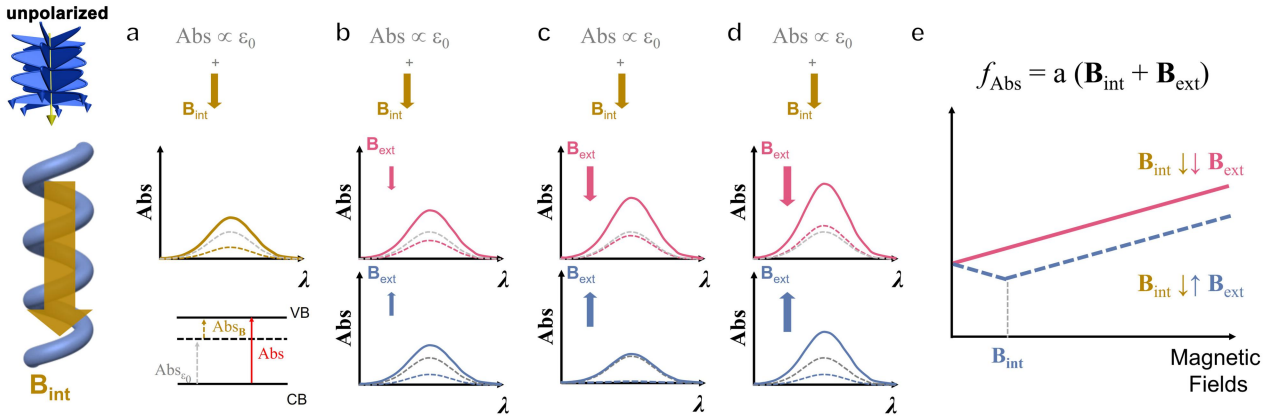

Figure S18. | Schematic representation for the light absorption behavior of chiral materials under various external magnetic fields ($\mathbf{B}_{ext}$). **a,** Intrinsic magnetic field of chiral materials, induced by electron movement under light irradiation, denoted as internal magnetic field ($\mathbf{B}_{int}$). **b,** $\mathbf{B}_{int} > \mathbf{B}_{ext}$. **c,** $\mathbf{B}_{int} = \mathbf{B}_{ext}$. **d,** $\mathbf{B}_{int} < \mathbf{B}_{ext}$. **e,** A schematic diagram showing the variation of the Abs with $\mathbf{B}_{ext}$, where their relationship is simply expressed as a linear function: $f_{Abs} = a(\mathbf{B}_{int} + \mathbf{B}_{ext})$.

When a material is irradiated with unpolarized light, defined by its wavevector ***k***, in a magnetic field **B**, light absorption can be enhanced or reduced (ΔAbs)[3].

Figure S18a shows the absorption behavior for chiral materials itself. For chiral materials, a chirality-dependent $\mathbf{B}_{int}$ would be generated when photoelectrons transport the chiral structure. Its absorption spectrum is the sum of both intrinsic absorption ($Abs_{\varepsilon 0}$) and the absorption caused by the $\mathbf{B}_{int}$ ($Abs_{\mathbf{B}int}$), i.e., $Abs = Abs_{\varepsilon 0} + Abs_{\mathbf{B}int}$. Therefore, the Abs of chiral materials is always higher than that of achiral ones.

Figure S18b-d show the chiral materials' absorption behavior with $\mathbf{B}_{ext}$. When $\mathbf{B}_{int} > \mathbf{B}_{ext}$, Abs would be slightly enhanced and reduced when $\mathbf{B}_{ext}$ and $\mathbf{B}_{int}$ are parallel ($\mathbf{B}_{int}\downarrow\downarrow\mathbf{B}_{ext}$) and antiparallel ($\mathbf{B}_{int}\downarrow\downarrow\mathbf{B}_{ext}$) each other, respectively. When $\mathbf{B}_{int} = \mathbf{B}_{ext}$, Abs would be increased significantly with $\mathbf{B}_{int}\downarrow\downarrow\mathbf{B}_{ext}$, and decreased significantly with $\mathbf{B}_{int}\uparrow\downarrow\mathbf{B}_{ext}$, with reaching minimum point. When $\mathbf{B}_{int} < \mathbf{B}_{ext}$, Abs is mainly influenced by $\mathbf{B}_{ext}$, with $\mathbf{B}_{int}\downarrow\downarrow$ $\mathbf{B}_{ext}$ alignment showing slightly greater enhancement than $\mathbf{B}_{int}\uparrow\downarrow\mathbf{B}_{ext}$.

Figure S18e illustrates the variation of Abs in chiral materials with $\mathbf{B}_{int}$ under different $\mathbf{B}_{ext}$. For simplicity, this relationship is represented using a linear approximation: the Abs with $\mathbf{B}_{int}\downarrow\downarrow\mathbf{B}_{ext}$ is consistently higher than that with $\mathbf{B}_{int}\uparrow\downarrow\mathbf{B}_{ext}$. Abs is increased with increasing magnetic fields strength under $\mathbf{B}_{int}\downarrow\downarrow\mathbf{B}_{ext}$, while the Abs shows the minimum point at $\mathbf{B}_{ext} = \mathbf{B}_{int}$ under $\mathbf{B}_{int}\uparrow\downarrow\mathbf{B}_{ext}$, and *vice versa* in opposite handedness.

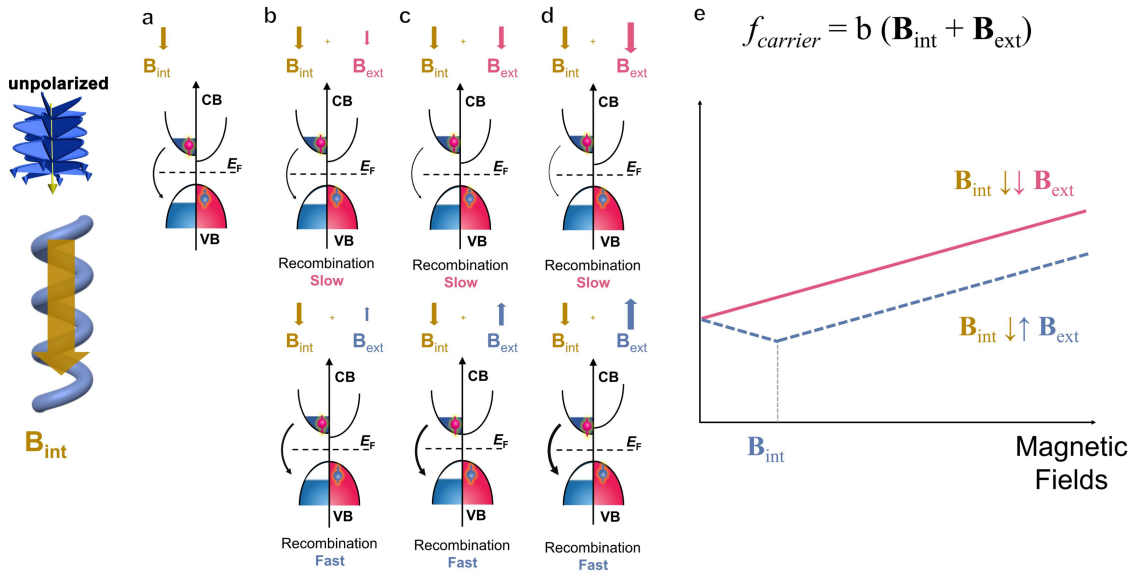

Figure S19. Schematic drawing of spin polarization suppressing photocarrier recombination in chiral materials under different B_{ext}. **a,** chiral materials itself having only $\mathbf{B}_{int}$. **b,** $\mathbf{B}_{int} > \mathbf{B}_{ext}$. **c,** $\mathbf{B}_{int} = \mathbf{B}_{ext}$. **d,** $\mathbf{B}_{int} < \mathbf{B}_{ext}$. **e,** A schematic diagram showing the variation of the material's photogenerated carrier utilization efficiency ($\eta_{carrier}$) with $\mathbf{B}_{ext}$, where their relationship is simply expressed as a linear function: $f_{carrier} = b(\mathbf{B}_{int} + \mathbf{B}_{ext})$.

The magnetic field causes energy level splitting in the material, making it more difficult for photoelectrons to recombine with photo-holes. This effect is dependent on the strength of the magnetic field. It is known that the photoexcited electrons should satisfy the conservation of spin angular momentum[4,5]. It can be predicted that the electrons in the CB undergo spin flipping and are inversed from their original spin direction during the charge-transfer process due to the strong asymmetric spin obit coupling in the chiral materials[4,6,7]. The spin-UP polarized photoexcited electrons are inversed to spin-DOWN, and *vice versa* in the chiral materials with

opposite handedness. These electrons cannot return to the VB due to spin filter channels and remain in the CB as free electrons and are utilized for photocatalysis[5,7]. Thus, the lifetimes of photocarriers and photocurrent density for a single spin type in chiral materials are greater than those in achiral materials without spin polarization.

Figure S19a shows the carrier behavior for chiral materials itself. Due to the presence of the $\mathbf{B}_{int}$ in chiral materials, their CB undergoes energy splitting, the carrier recombination rate decreases with the increase in energy level, thereby enhancing the $\eta_{carrier}$. Therefore, the carrier lifetime of chiral materials is always longer than that of achiral ones.

Figure S19b-d show chiral materials' carrier behavior with $\mathbf{B}_{ext}$. When $\mathbf{B}_{int} > \mathbf{B}_{ext}$, $\eta_{carrier}$ would be slightly enhanced and reduced with $\mathbf{B}_{int}\downarrow\downarrow\mathbf{B}_{ext}$ and $\mathbf{B}_{int}\uparrow\downarrow\mathbf{B}_{ext}$, respectively. When $\mathbf{B}_{int} \approx \mathbf{B}_{ext}$, $\eta_{carrier}$ would be increased significantly with $\mathbf{B}_{int}\downarrow\downarrow\mathbf{B}_{ext}$, and decreased significantly with $\mathbf{B}_{int}\uparrow\downarrow\mathbf{B}_{ext}$, with reaching minimum point. When $\mathbf{B}_{int} < \mathbf{B}_{ext}$, $\eta_{carrier}$ is mainly influenced by $\mathbf{B}_{ext}$, with $\mathbf{B}_{int}\downarrow\downarrow\mathbf{B}_{ext}$ alignment showing slightly greater enhancement than $\mathbf{B}_{int}\uparrow\downarrow\mathbf{B}_{ext}$.

Figure S19e illustrates the variation of $\eta_{carrier}$ in chiral materials with $\mathbf{B}_{int}$ under different $\mathbf{B}_{ext}$ conditions. For simplicity, this relationship is represented using a linear approximation: the $\eta_{carrier}$ with $B_{int}\downarrow\downarrow B_{ext}$ is consistently higher than that with $\mathbf{B}_{int}\uparrow\downarrow\mathbf{B}_{ext}$. $\eta_{carrier}$ is increased with increasing magnetic fields strength under $B_{int}\downarrow\downarrow B_{ext}$, while the $\eta_{carrier}$ shows the minimum point at $\mathbf{B}_{ext} = \mathbf{B}_{int}$ under $\mathbf{B}_{int}\uparrow\downarrow\mathbf{B}_{ext}$, and *vice versa* in opposite handedness.

Mechanism of differences in the yields of amino acids under external magnetic fields

The different yields of amino acids under different magnetic fields can be explained in terms of the light absorption properties and charge carrier behavior of pyrite in the presence of a magnetic field.

As mentioned above, the Abs and carrier behavior of chiral materials exhibit the same trend with similar relationships between their efficiency and magnetic fields. The photocatalytic reaction efficiency ($\boldsymbol{f}_{photo}$) on the pyrite surface is jointly influenced by Abs and carrier utilization efficiency $\boldsymbol{\eta}_{carrier}$. The variation of $\boldsymbol{f}_{photo}$ with magnetic field is simply represented by a linear equation: $f_{photo} = c(\mathbf{B}_{sur} + \mathbf{B}_{chiral} + \mathbf{B}_{ext})$ (Figure S20). In NP and SP, $\mathbf{B}_{int} = \mathbf{B}_{sur}$, in which $\mathbf{B}_{sur}$ represents the magnetic field generated when electrons move through the wavy arrangement of atoms on the pyrite surface. In CMP, $\mathbf{B}_{int} = \mathbf{B}_{sur} + \mathbf{B}_{chiral}$, in which $\mathbf{B}_{chiral}$ refers to the magnetic field produced as electrons travel along the chiral mesostructure in CMP.

Without $\mathbf{B}_{ext}$:

For NP and SP, $f_{photo} = c(\mathbf{B}_{sur})$, and for CMP, $f_{photo} = c(\mathbf{B}_{sur} + \mathbf{B}_{chiral})$. Obviously, the $\boldsymbol{f}_{photo}$ of CMPs is higher than that of NP and SP. Since $\mathbf{B}_{sur} << \mathbf{B}_{chiral}$, the $\mathbf{B}_{int}$ of D-CMP and L-CMP is nearly equal in magnitude but opposite in direction. Without $\mathbf{B}_{ext}$, the $\boldsymbol{f}_{photo}$ values follow the order: D-CMP ≈ L-CMP >> SP ≈ NP. Considering additional factors such as catalyst particle size and morphology in real reactions, the Ala yield shows the following trend: D-CMP ≈ L-CMP >> SP > NP.

With $\mathbf{B}_{ext}$:

As shown in Figure S20a, for NP and SP, as $\mathbf{B}_{int} = \mathbf{B}_{sur}$, thus $f_{photo} = c(\mathbf{B}_{sur} + \mathbf{B}_{ext})$. Because $\mathbf{B}_{sur}$ is relatively weak, only conditions where $\mathbf{B}_{ext} > \mathbf{B}_{sur}$ were observed. Under these conditions, the yield of Ala gradually increases from 0 to 1.5 T, and the yield under parallel alignment of $\mathbf{B}_{sur}$ and $\mathbf{B}_{ext}$ is consistently higher than that under antiparallel alignment. The yields of Ala were increased significantly with $\mathbf{B}_{int}\downarrow\downarrow\mathbf{B}_{ext}$, and slightly increased with $\mathbf{B}_{int}\uparrow\downarrow\mathbf{B}_{ext}$.

As shown in Figure S20b, for D-CMP, due to its helical chiral mesostructure, generates a stronger $\mathbf{B}_{chiral}$. Given that $\mathbf{B}_{chiral} >> \mathbf{B}_{sur}$, the internal field can be approximated as $\mathbf{B}_{int} \approx \mathbf{B}_{chiral}$. When $\mathbf{B}_{int} > \mathbf{B}_{ext}$, the yields of Ala on the D-CMP were increased and decreased with increasing $\mathbf{B}_{ext}$ from 0 to 1.5 T under $\mathbf{B}_{int}\downarrow\downarrow\mathbf{B}_{ext}$ and $\mathbf{B}_{int}\uparrow\downarrow\mathbf{B}_{ext}$, respectively, and *vice versa* on the L-CMP.

It is worth noting that the schematic diagrams serve only to qualitatively illustrate the relative f_{photo} values under different magnetic field directions and the general trend with increasing field strength. They are not intended to precisely match the experimental results. In practice, the combined effects of magnetic fields on Abs and $\eta_{carrier}$, and thereby on r_{photo}, are more complex and require further kinetic investigation.

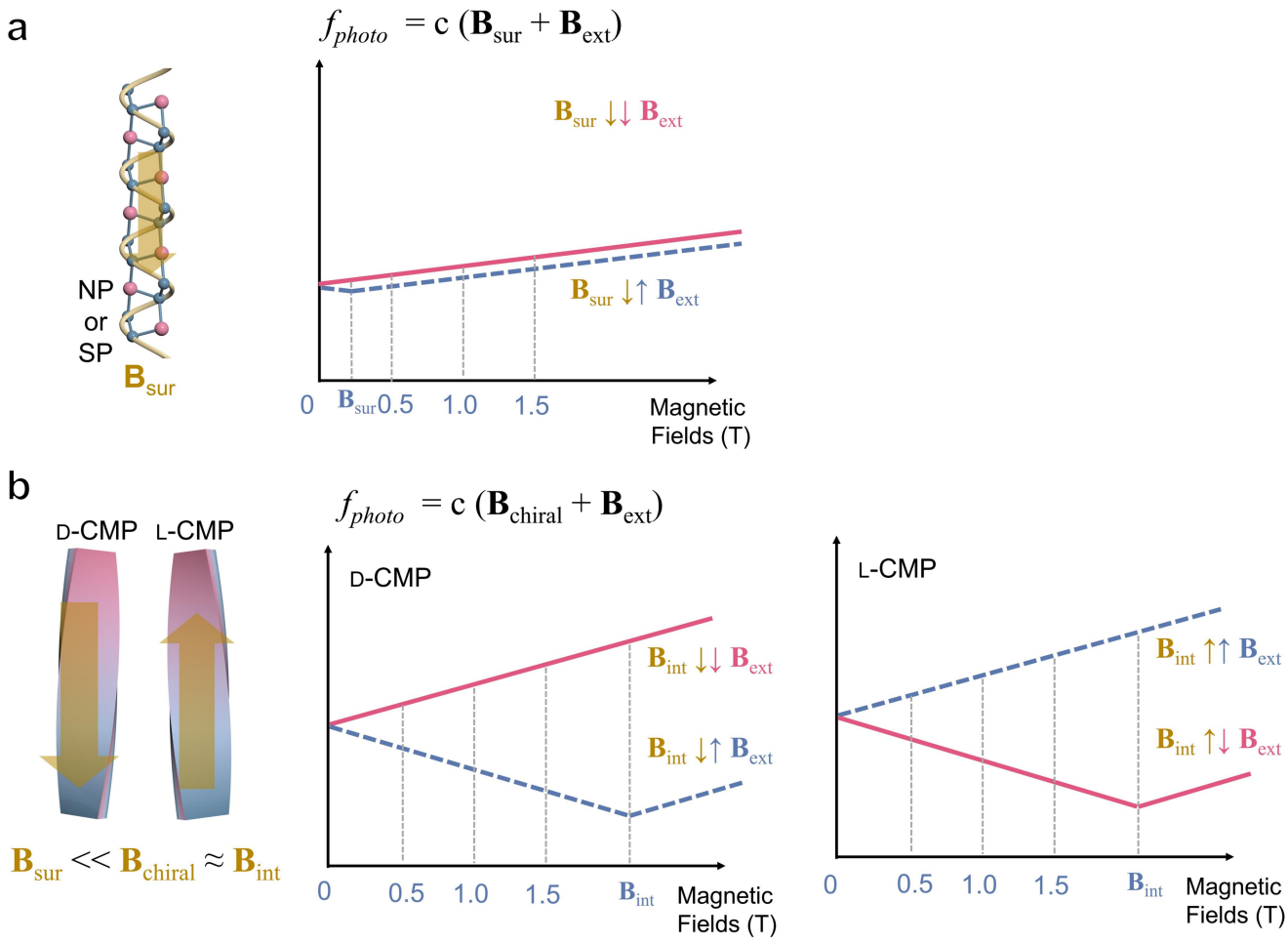

Figure S20. Schematic representation of the relationships between the efficiency of photoreaction (f_{photo}) and magnetic fields. **a**, NP and SP. **b**, D- and L-CMPs.

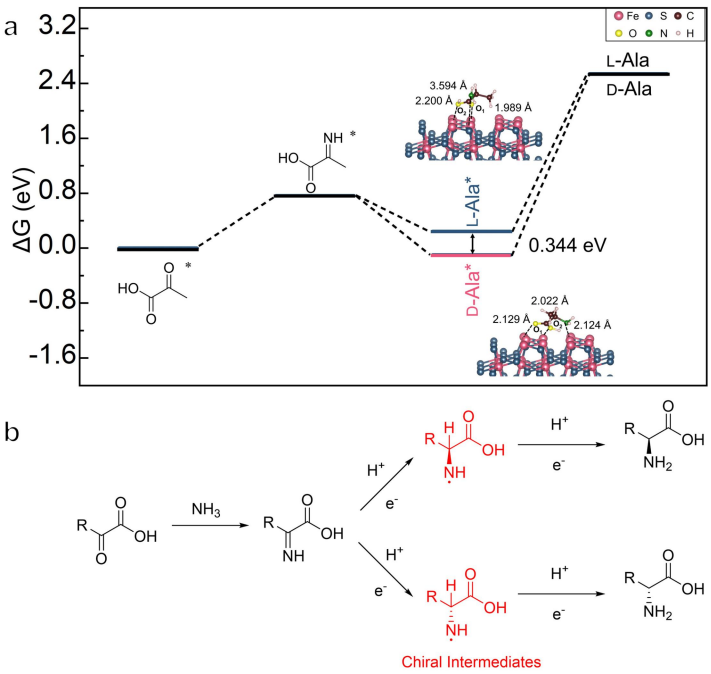

Figure S21. Mechanism of resistance of pyrite enantioselectivity for amino acids to CDFs. **a,** Gibbs free energy profile of the intermediates for the formation of D-/L-Ala on (200) surface of pyrite[8]. **b,** Reaction process of amino acid by amination of *α*-keto acid[9].

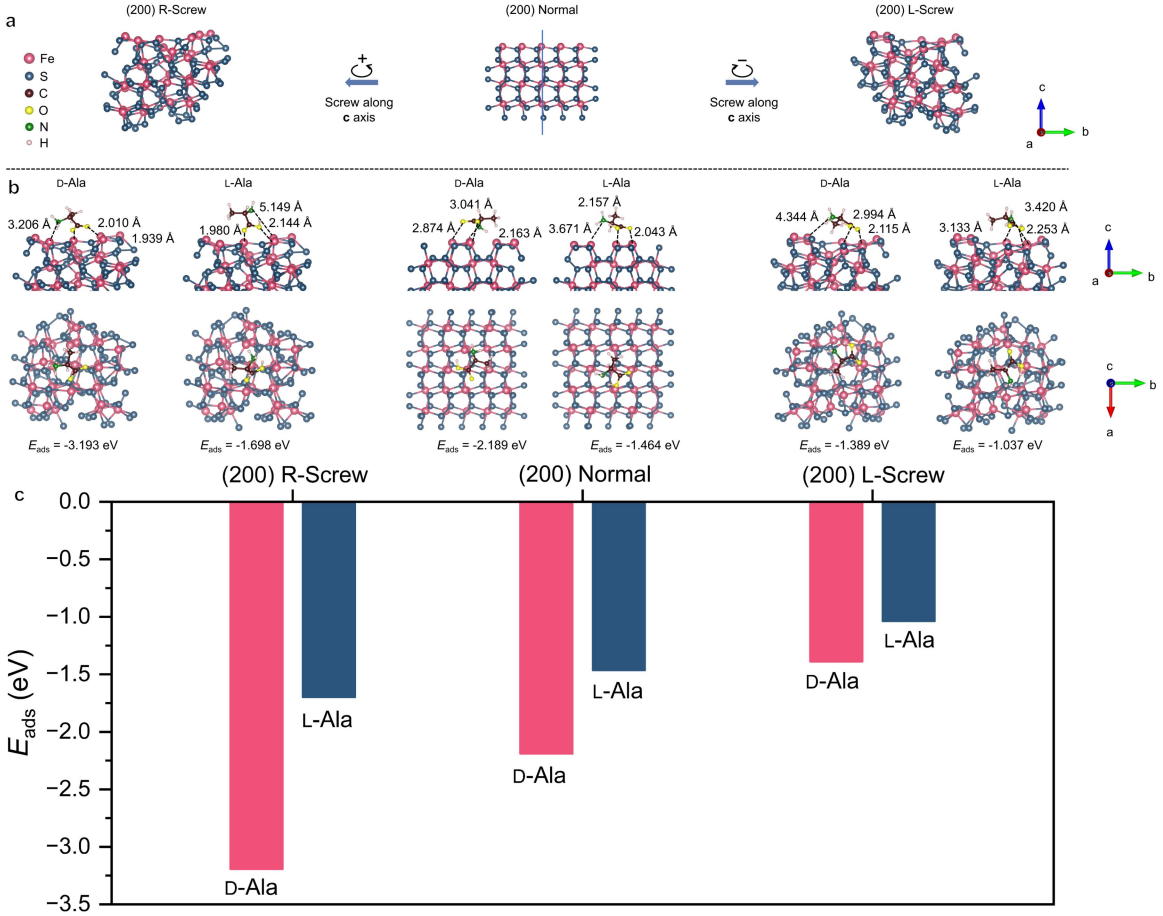

Figure S22. The adsorption energies of D- and L-Ala on the screw pyrite (200) crystal surface predicted by DFT calculations. **a,** The (200) crystal surface forms twisted facets along different directions of the *c*-axis, with the crystal facets rotated by a positive angle labeled as R-Screw, and those rotated by a negative angle labeled as L-Screw. **b,** Adsorption models of D- and L-Ala on different (200) crystal surfaces. **c,** Adsorption energy of D- and L-Ala on the R- and L-screw and normal pyrite (200).

To investigate the influence of chiral mesostructures on enantioselectivity, DFT calculations were conducted to evaluate the adsorption energy on the screw surface. Two enantioselectivity factors are present on the screw surface: the wavy atomic arrangement of the pyrite surface and the chiral distortion of the crystal plane. As depicted in Figure S22a, the (200) crystal plane was distorted along the c-axis to simulate the chiral distortion of CMP, and its mirror image was utilized to represent the opposite chiral distortion, labeled as R-Screw and L-Screw, respectively. The undistorted crystal plane is designated as Normal. As illustrated in Figure S22b-c, the Normal crystal surface exhibits a significant difference in adsorption energy for D- and L-Ala (0.725 eV), indicating that the atomic arrangement of the (200) crystal plane inherently favors D-Ala. The R-Screw surface shows an even larger difference in adsorption energy (1.495 eV), suggesting that the R-screw also selects D-Ala. This selectivity is superimposed on the intrinsic selectivity of pyrite, thereby increase the difference between D-Ala and L-Ala. In contrast, the L-Screw surface, with the opposite chiral twist, shows a smaller difference in adsorption energy (0.361 eV), indicating that the L-screw selects L-Ala. This selection counteracts the intrinsic selectivity of pyrite and decrease the difference between D-Ala and L-Ala. However, the overall selectivity of this crystal plane remains for D-Ala.

However, it is worth noting that the screw models have more exaggerated distortion compared to the CMP observed in the TEM images. In spite of this, the right- and left-handed helices still do not overweigh intrinsic enantioselectivity of pyrite in DFT calculation. Therefore, the chiral distortions present in CMP are unlikely to invert the enantioselectivity of the pyrite surface, which leads to both D- and L-CMP surfaces selected D-Ala in catalytic experiments.

Note: To facilitate comparison, the theoretical calculations in this study utilized the D3 dispersion correction. While the D4 dispersion correction method used in our previous work[3] considers additional charge-related factors[5], it has proven inadequate for dealing with irregular crystal plane models like R-Screw and L-Screw. Furthermore, it has been shown that employing the D3 dispersion correction does not impact the evaluation of enantioselectivity. Consequently, the D3 dispersion correction is considered the most suitable option here.

Table S1. The binding energy of S-S or the functional groups in amino acids (-COOH, -NH_2, -SH) coordinated with Fe atoms, as predicted by DFT calculations.

Fe O S N C H	Molecular model with Fe	Distance (Å)	BE (eV)
$Fe\text{-}S_2$		2.063 2.236	-4.903
Fe-SH_Cys	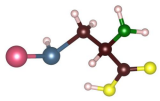	2.021	-1.630
Fe-COOH_Ala	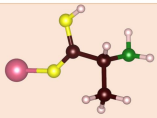	1.791	-1.178
$Fe\text{-}NH_2$_Ala	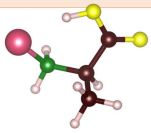	1.917	-1.829

To investigate the coordination behavior of chiral amino acid molecules on the pyrite surface, the binding energies of the S-S bond and various functional groups (including -SH, -COOH and -NH_2) with Fe atoms were computed. As shown in Table S1, the binding energy between Fe and the S-S bond was found to be -4.903 eV, while the binding energies of the other functional groups were -1.630 eV, -1.178 eV, and -1.829 eV, respectively. Fe atoms exhibit the lowest binding energy with S-S bonds, indicating the high stability of Fe-S bonds in pyrite. Consequently, (i) the wave-like atomic arrangement of the pyrite surface remains intact and is not replaced by organic chiral molecules, and (ii) Fe-chiral molecule complexes are difficult to be formed.

References

1.Andrews SS, Tretton J. Physical principles of circular dichroism. J Chem Educ. 2020;97(12):4370-4376. [DOI:10.1021/acs.jchemed.0c01061]

2.Ding K, Ai J, Deng Q, Huang B, Zhou C, Duan T, et al. Chiral mesostructured BiOBr films with circularly polarized colour response. Angew Chem Int Ed. 2021;133(35):19172-19177. [DOI:10.1002/anie.202105496]

3.Ishii K, Hattori S, Kitagawa Y. Recent advances in studies on the magneto-chiral dichroism of organic compounds. Photochem Photobiol Sci. 2020;19(1):9-19. [DOI:10.1039/c9pp00400a]

4.Ai M, Pan L, Shi C, Huang ZF, Zhang X, Mi W, et al. Spin selection in atomic-level chiral metal oxide for photocatalysis. Nat Commun. 2023;14(1):4562. [DOI:10.1038/s41467-023-40367-x]

5.Gao W, Peng R, Yang Y, Zhao X, Cui C, Su X, et al. Electron spin polarization-enhanced photoinduced charge separation in ferromagnetic $ZnFe_2O_4$. ACS Energy Lett. 2021;6(6):2129-2137. [DOI:10.1021/acsenergylett.1c00682]

6.Mtangi W, Tassinari F, Vankayala K, Vargas Jentzsch A, Adelizzi B, Palmans AR, et al. Control of electrons' spin eliminates hydrogen peroxide formation during water splitting. J Am Chem Soc. 2017;139(7):2794-2798. [DOI:10.1021/jacs.6b12971]

7.Lin CC, Liu TR, Lin SR, Boopathi KM, Chiang CH, Tzeng WY, et al. Spin-polarized photocatalytic CO_2 reduction of Mn-doped perovskite nanoplates. J Am Chem Soc. 2022;144(34):15718-15726. [DOI:10.1021/jacs.2c06060]
8.Li R, Deng Q, Han L, Ouyang T, Che S, Fang Y. Prebiotic formation of enantiomeric excess D-amino acids on natural pyrite. Nat Commun. 2024;15(1):10130. [DOI:10.1038/s41467-024-54481-x]
9.Cui Y, Ai J, Duan Y, Jia M, Ouyang T, Liu A, Yu L, Liu J, Liu X, Chu C, Li Y. Enantioselective synthesis of amino acids by photocatalytic reduction of CO_2 on chiral mesostructured ZnS. Chem. 2025;11(5):102390. [DOI:10.1016/j.chempr.2024.102390]